ADVANCED MATERIALS
www.advmat.de

Shortwave Infrared Light Detection and Ranging Using Silver Telluride Quantum Dots

*Yongjie Wang, Hao Wu, Carmelita Rodà, Lucheng Peng, Nima Taghipour, Miguel Dosil, and Gerasimos Konstantatos**

Shortwave infrared (SWIR) light, characterized as the "eye-safe" window, is considered extremely promising in various technological fields and particularly valuable for imaging and light detection and ranging (LiDAR) applications. Silver telluride (Ag_2Te) colloidal quantum dots (CQDs), featuring RoHS-compliance, solution-processability, and CMOS compatibility, emerge as a potential contender for SWIR optoelectronics. Yet, further improvements in dark current, response speed, and linear dynamic range (LDR) are essential for meeting the rigorous demands of sensing and LiDAR applications. Here, it is shown that post-synthesis surface engineering and doping control significantly improve the dark current, response speed, and LDR of Ag_2Te CQD photodiodes, achieving a low dark current of 450 nA cm^{-2} at −0.5 V, an LDR exceeding 150 dB, and a rapid response speed of ≈25 ns. A proof-of-concept LiDAR demonstration in the SWIR using a practical nanosecond diode laser achieves decimetre-level resolution at a distance exceeding 10 m. This work represents a key step in advancing SWIR CQDs toward consumer electronics and automotive markets.

1. Introduction

Among the various wavelengths of light, the shortwave infrared (SWIR) region holds particular importance due to its unique properties. SWIR light experiences less scattering in the atmosphere, compared to visible light,[1,2] allowing greater penetration depth, especially in adverse weather conditions. Moreover, in the SWIR there exist spectral bands that are free of ambient background solar light, enabling ubiquitous operation of sensing and ranging during day and night. Last but not least, SWIR light is mostly absorbed by the cornea,[3–5] minimizing the risk of retinal damage even at high power levels, rendering it "eye-safe." All of the above make SWIR a particularly valuable spectral range for a vast range of applications including LIDAR, 3D-imaging, space localization and mapping (SLAM), and machine vision.

Currently, SWIR photodetectors primarily rely on epitaxial bulk semiconductors, which come with high cost and low manufacturing throughput. Over the past decades, colloidal quantum dots (CQDs) have emerged as a promising new class of materials for infrared detectors, thanks to their extraordinary optoelectronic properties. Efforts have been dedicated predominately to lead- or mercury-based chalcogenide CQDs,[6–11] though their heavy-metal toxicity poses significant challenges to commercial adoption. Recently, the demand for Restriction of Hazardous Substances (RoHS) compliant SWIR materials has shifted attention toward heavy-metal-free CQDs, such as indium arsenide (InAs),[12–15] indium antimonide (InSb),[16–18] silver telluride (Ag_2Te),[19–21] and silver selenide (Ag_2Se)[2,22,23] CQDs, offering an environmentally friendly path for SWIR optoelectronics and easy market adoption.

Although still in its infancy, Ag_2Te CQDs have shown promising device performance at high frequencies, comparable to those of their toxic counterparts.[19,21] However, for practical applications and integration with read-out electronics, it is the low-frequency regime (≈1 Hz) that determines mostly the final performance of the photodetector, which is currently suffering primarily from a high dark current. Furthermore, for demanding applications like LiDAR, wide linear dynamic range (LDR) and fast response speed are prerequisites to operate with objects of various reflectivities and distances.[24] Hence, substantial improvements in dark current, LDR, and response speed are urgently needed to increase the technology readiness level for practical applications.

Here, in this work, we report on the surface engineering of Ag_2Te CQDs with tight-binding thiols, enabling improved colloidal stability, longer carrier lifetime, and higher photoluminescence quantum yield (PLQY). Furthermore, we have engineered

Y. Wang, H. Wu, C. Rodà, L. Peng, N. Taghipour, M. Dosil, G. Konstantatos
The Barcelona Institute of Science and Technology
ICFO-Insitut de Ciencies Fotoniques
Castelldefels, Barcelona 08860, Spain
E-mail: Gerasimos.Konstantatos@icfo.eu
G. Konstantatos
ICREA-Institució Catalana de Recerca i Estudiats Avançats
Lluis Companys 23, Barcelona 08010, Spain

The ORCID identification number(s) for the author(s) of this article can be found under https://doi.org/10.1002/adma.202500977

DOI: 10.1002/adma.202500977

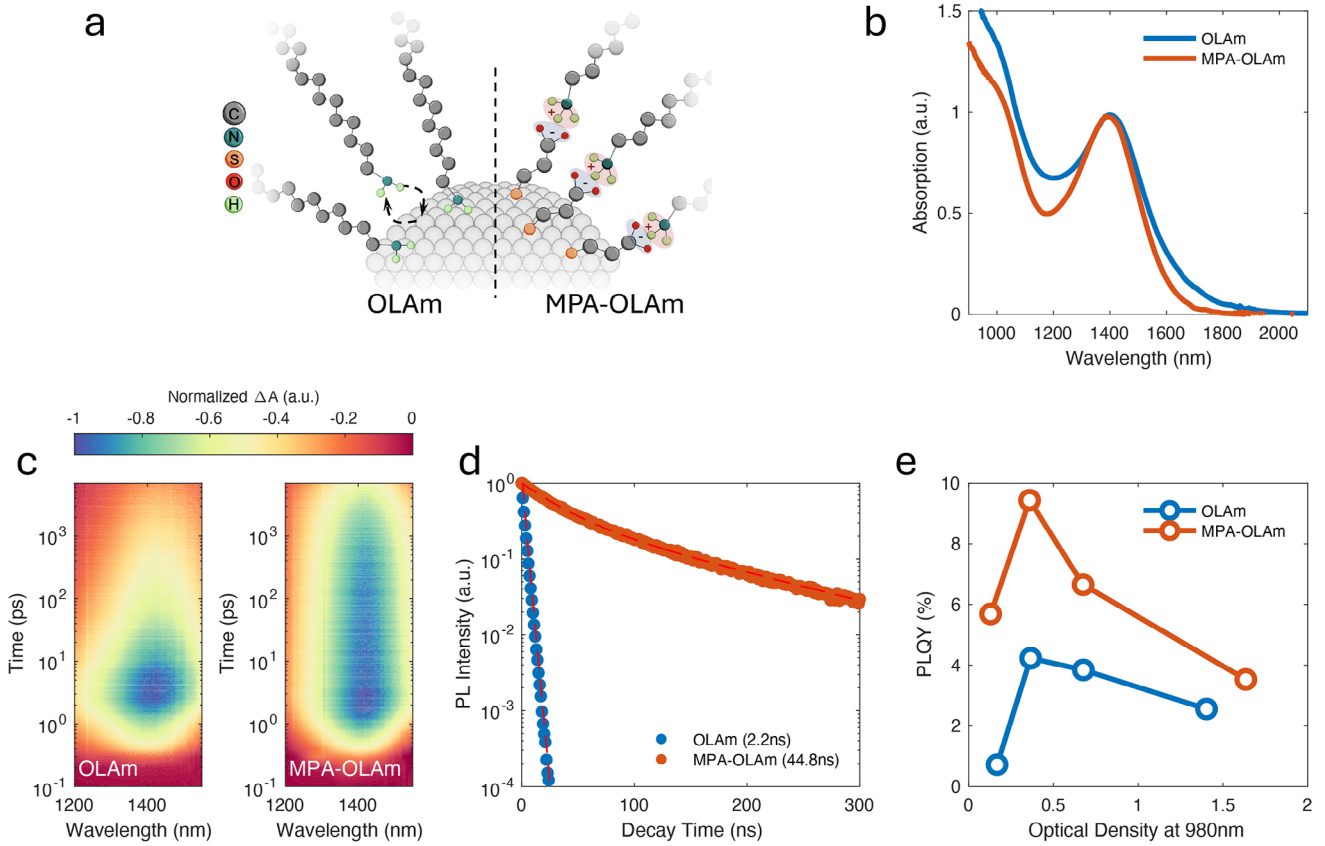

Figure 1. Surface Engineering with Tight-binding Thiols. a) Schematics of QD surface without (*OLAm*) and with (*MPA-OLAm*) tight-binding MPA ligands. b) Absorption spectra of *OLAm* and *MPA-OLAm* capped Ag_2Te QD solutions. c) Transient absorption contour plots of *OLAm* and *MPA-OLAm* QD solutions. d) transient PL decays of *OLAm* and *MPA-OLAm* capped Ag_2Te QD solutions. e) PLQYs of *OLAm* and *MPA-OLAm* capped Ag_2Te QD solutions at different concentrations.

doping on CQD films by introducing a new cationic ligand of silver nitrate ($AgNO_3$) in order to further optimize the quantum-dot stack of the photodiode (PD). The resultant SWIR photodiode devices exhibit a dark current of 450 nA cm^{-2} at −0.5 V, EQE of over 30%, LDR exceeding 150 dB, and a fast response time of ≈25 ns. Leveraging those photodiode characteristics, proof-of-concept SWIR LiDAR was further demonstrated using fast-response Ag_2Te QD PDs with an "eye-safe" 1310 nm semiconductor diode nanosecond laser. The result here remarks, to the best of our knowledge, the first SWIR LiDAR using solution-processed, RoHS-compliant materials, paving the way for CQD SWIR PDs toward the consumer and automotive electronics market.

1.1. Surface Engineering with Tight-Binding Thiols

Silver telluride quantum dots (Ag_2Te QDs) were first synthesized following our previously reported method,[21] as the oleylamine (OLAm) capped samples. It was observed that *OLAm* capped QDs in solution undergo peak-broadening at low concentrations (Figure S1, Supporting Information), which is presumably due to the weak and dynamic binding characteristics of OLAm with metal halides on QD surfaces,[25–27] leading to QD fusing and agglomerating in solution with long-term storage. We posited that a tighter surface-ligand binding scheme is necessary for better colloidal stability and surface passivation. 3-mercaptopropionic acid (MPA), a bifunctional thiol ligand,[19,20,28] has been proven to form bound ion pair MPA-OLAm as the hybrid ligands for PbS and HgTe CQDs, improving the colloidal stability and solution processability.[9,29] We thus introduced MPA-OLAm as the tighter surface-ligand binding ligands than OLAm-only for Ag_2Te CQDs. As illustrated in **Figure 1a**, the thiol group is proposed to bind with Ag cations on the QD surface, while the carboxyl group reacts with oleylamine, forming carboxylate ammonium ion pairs as long-chain ligands to warrant colloidal stability (Figures S2 and S3, Supporting Information). Figure 1b shows the QDs' absorption spectra of two different ligands, where the *MPA-OLAm* capped QDs displayed a narrower peak, indicating the efficacy of MPA post-synthesis treatment. Furthermore, transmission electron microscopy (TEM) imaging confirms that *OLAm* QDs comprise QD agglomerates, while *MPA-OLAm* capped samples display unambiguously well separated and dispersed individual QDs (Figure S4, Supporting Information).

To better understand the surface-ligand related passivation effects, charge carrier dynamics were further investigated via transient absorption spectroscopy. As shown in Figure 1c, *MPA-OLAm* capped QDs showed a ground state bleach (GSB) lifetime much longer than the *OLAm* QDs, indicating improved

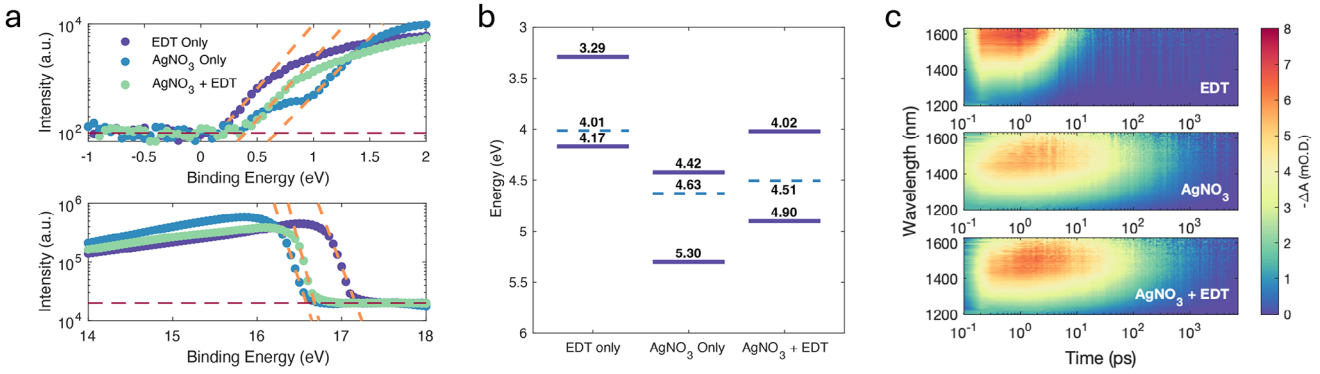

Figure 2. Doping control of Ag_2Te QD films. a) UPS spectra of Ag_2Te QD films treated with EDT-only, $AgNO_3$-only and $AgNO_3$ + EDT ligands. b) Band levels of Ag_2Te QD films treated with EDT-only, $AgNO_3$-only and $AgNO_3$ + EDT ligands. c) Transient absorption contour plots of Ag_2Te QD films treated with EDT-only, $AgNO_3$-only and $AgNO_3$ + EDT ligands.

surface passivation and reduced trap-states after *MPA-OLAm* treatment.[30,31] In addition, as shown in Figure 1d,e, *MPA-OLAm* QDs presented a longer photoluminescence (PL) lifetime (44.8vs 2.2 ns), resonating with the improved GSB lifetime. In order to evaluate the photoluminescence quantum yield (PLQY), smaller size QDs were used for PL measurements (Figure S5, Supporting Information) to avoid reaching the detector range limit (≈1600 nm). As shown in Figure 1e, higher PLQY by a factor of two (9.5% vs 4.2%) was obtained upon *MPA-OLAm* treatment, further confirming the improved surface passivation with tightly binding thiol ligands.

1.2. Doping Control of Ag_2Te QD films

With improved surface passivation, we sought to build QD films from the *MPA-OLAm* capped QDs. 1,2-ethandithiol (EDT) was employed first as an effective ligand-exchange agent. However, QD films showed a heavy *p*-type doping property, consistent with our previous report.[21] The lack of control over the doping levels leads to severe interface recombination, posing restrictions on device structure design and optimization.[32–35] We hypothesized that doping of Ag_2Te CQDs, which previously exhibited very high *p*-type doping, could be tuned via the introduction of Ag ions giving a more *n*-type character. Therefore, we introduced a cationic ligand, silver nitrate ($AgNO_3$), functioning not only as an exchanging ligand for Ag_2Te QDs (Figure S6, Supporting Information), but also as an effective *n*-type dopant. After treating with $AgNO_3$, UV photoelectron spectra (UPS) revealed a *n*-type doping feature (**Figure 2**a,b), in contrast to EDT-treated-only films. Moreover, films treated with $AgNO_3$ + EDT showed a weak p-doping property, confirming the effectiveness of doping control with $AgNO_3$ treatment. The doping densities were further estimated to be (p) 3×10^{17} cm^{-3}, (n) 3×10^{16} cm^{-3} and (p) 2×10^{13} cm^{-3} for EDT-only, $AgNO_3$-only and $AgNO_3$ + EDT treated films, respectively (Note S1, Supporting Information). X-ray photoelectron spectroscopy (XPS) further corroborates the increased Ag/Te ratio (Figure S7, Supporting Information) after $AgNO_3$ treatment, in accordance with previous reports of *n*-type doped silver selenide QDs.[23,36,37] As a result, QD films with $AgNO_3$ treatment showed a narrower absorption peak (Figure S8, Supporting Information) and a much longer GSB lifetime than EDT only films, as shown in Figure 2c, indicating the reduction of band-edge tail states and trap-assisted Auger recombination.[38,39]

1.3. Shortwave Infrared Photodiodes

Leveraging the advances in the material properties we fabricated photodiode devices with a configuration of ITO/SnO_2/Ag_2Te-$AgNO_3$/Ag_2Te-$AgNO_3$ + EDT/Au (**Figure 3**a) to assess their anticipated improvements in device performance. Figure 3b shows the well-aligned band positions of the device structure. In order to investigate the device structure and doping effects on diode quality and dark-currents, temperature-dependent current–density voltage (*J–V*) measurements were further conducted. EDT-only devices showed nearly unaffected *J–V* curves under different temperatures (Figure S9, Supporting Information), likely due to high doping density and trap-mediated transport channel.[40–42] On the contrary, devices with $AgNO_3$ + EDT ligands showed proper diode behaviors and a clear reduction of reverse dark current with temperature decreasing (Figure 3c), indicating a thermally activated process dominating dark current. Analysis of the temperature-dependent *J–V* curves revealed that $AgNO_3$ + EDT devices showed an activation energy ≈0.3 eV, while EDT-only devices showed near zero activation energy, consistent with the almost unaltered *J–V* curves with temperature changes. Further analysis on the $AgNO_3$ + EDT devices uncovered that reverse dark-current was dominated by a trap-related leakage current (Figure S10 and Note S2, Supporting Information) along with a thermionic emission barrier ≈0.6 eV, presumably due to the Schottky barrier at QDs/Au interface.[43–45]

Ag_2Te CQDs SWIR photodiodes showed a dark current density of ≈450 nA cm^{-2} at −0.5 V reverse bias (**Figure 4**a), which is more than one order of magnitude lower than previous reports.[20,21,36] As shown in Figure 4b, devices also presented broad-band response from 350 nm to over 1600 nm, with a peak EQE over 20% under 0 V bias and 30% under −1 V bias at ≈1450 nm, matching well with simulated EQE (Figure S11, Supporting Information). Further statistical analysis of device performance revealed the dark current density@-0.5 V as 0.63 ± 0.17 μA cm^{-2} and peak EQE as 27 ± 4% (Figure S12, Supporting Information).

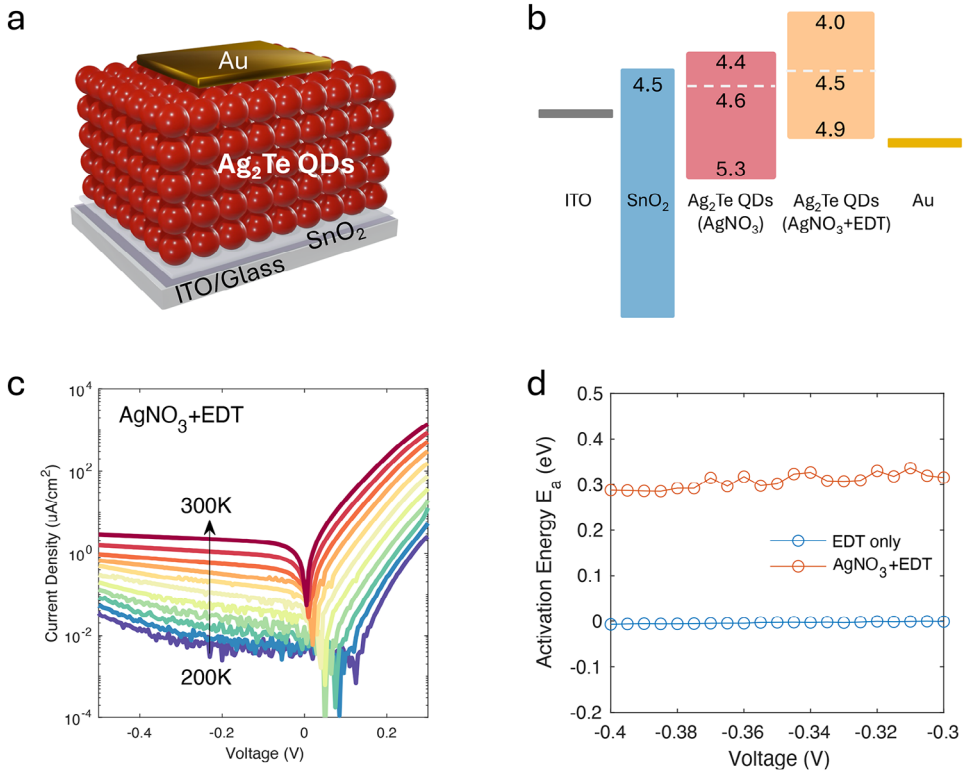

Figure 3. Shortwave Infrared Photodiodes. a) Schematic of the Ag_2Te QD photodiodes. b) Band diagram of the photodiode device. c) Temperature dependent dark current density–voltage (*J–V–T*) curves of photodiodes with $AgNO_3$ + EDT treatments. d) Activation energy of EDT-only and $AgNO_3$ + EDT devices extracted from *J–V–T* measurements.

The device also showed high stability under −1 V reverse bias, without apparent degradation for over 1h bias stress test (Figure S13, Supporting Information). Noise power spectral density was measured to properly assess the detection performance (Figure S14, Supporting Information). Frequency-dependent current noise spectrum of Ag_2Te QD photodiode reached ≈4.5 × 10^{-13} $A/\sqrt{Hz}$ at 1 Hz with a *1/f* noise at lower frequencies measured by the transient-current fast Fourier-Transform (FFT) method. The room-temperature specific detectivity was further calculated with:

$$D^* = \frac{R\sqrt{A\Delta f}}{i_n} \quad (1)$$

where A is the device area, R is the responsivity, Δf is the electrical bandwidth, and i_n is the noise spectral density. Figure 4c shows the spectral-specific detectivity at 1 Hz, where the D^* reached 10^{11} Jones at the SWIR region, which is an order of magnitude higher than previously.[21] Linear dynamic range (LDR) was measured with the $AgNO_3$ + EDT treated devices. As shown in Figure 4d, SWIR photodiode based on surface engineered Ag_2Te QDs showed a clear linearity between photocurrent and incident light across a wide range from ≈10^{-7} to ≈10 mW cm^{-2} and reached an LDR over 150 dB, which outperforms prior reports (Table S1, Supporting Information).[4,12,17–21,46–50] The directly measured noise equivalent power was found to be ≈2.5 pW at 1350 nm, in consistency with the measured specific detectivity.

Transient photocurrent (TPC) measurements were conducted to characterize the response time of Ag_2Te QD SWIR photodiodes. By analyzing the current transients of different device areas under 50 ns laser pulses (Figure S15, Supporting Information), the response time was found to decrease with device area reduction, indicating a geometrical capacitance limited response speed (Figure 4e).[4,51] The devices with an area of 10^4 um^2 reached ≈25 ns response time, which suggested an estimated mobility as >10^{-2} cm^2 $V{\cdot}s^{-1}$ (Note S3, Supporting Information). To further corroborate the response speed of our devices we measured frequency-dependent photo-response with 50% duty-cycle laser pulses (Figure 4f), which revealed an increase of −3 dB bandwidth with device area decreasing, reaching > 5 MHz at 10^4 um^2, consistent with the TPC measurements.

1.4. SWIR LiDAR Demo

Having achieved low dark current and fast response in our detectors, we further sought to apply them in demonstrating for the first time light detection and ranging (LiDAR) using CQD technology in the SWIR to optically measure an object's distance. Current standardized LiDAR techniques use methods such as pulsed time-of-flight (direct TOF), amplitude-modulated continuous wave (AMCW), and frequency-modulated continuous wave (FMCW) detection for range measurements. Here, we followed recent papers on LiDAR demonstration[24,52] and implemented the pulsed time-of-flight (direct TOF) method. LiDAR based on

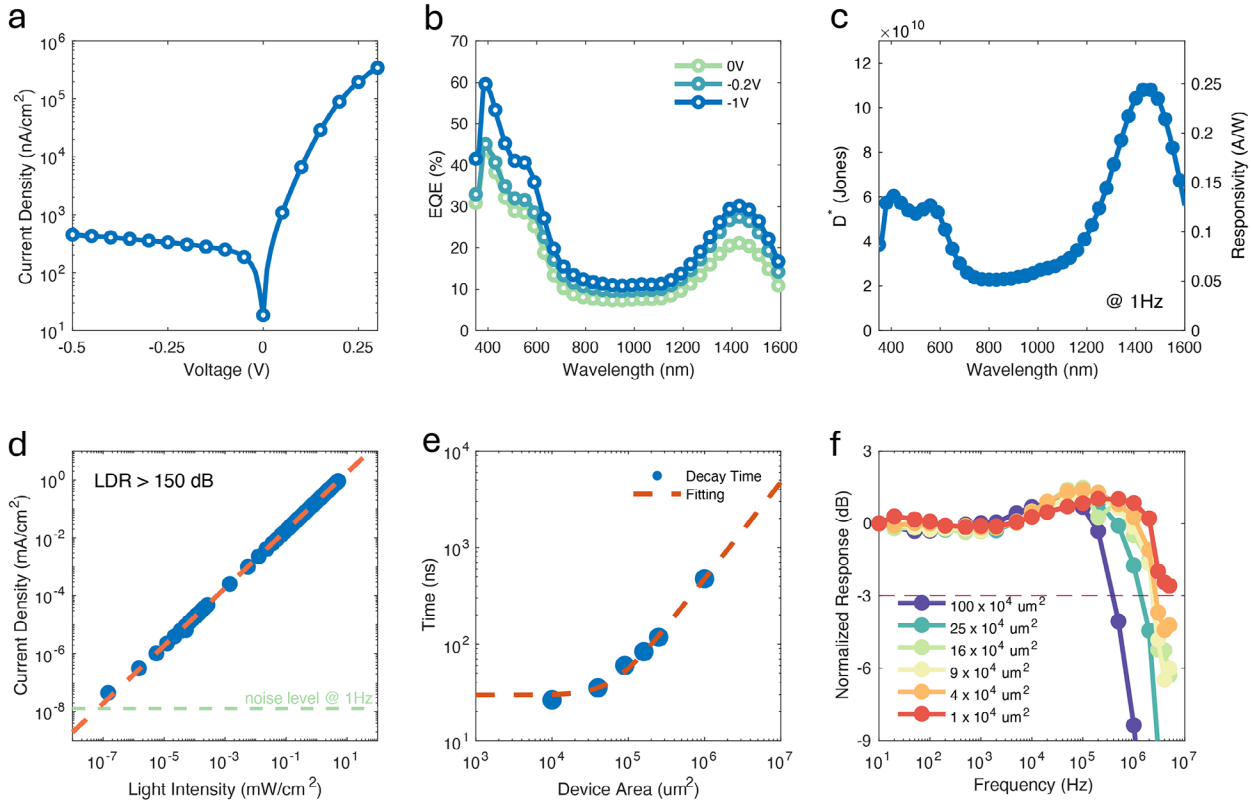

Figure 4. Photodiode device performance. a) dark current density–voltage curve of the champion device. b) EQE spectra under zero and −1 V bias of champion device. c) Specific detectivity (D^*) and Responsivity of champion device at 1Hz. d) Linear dynamic range (LDR) of Ag_2Te QD photodiode under 1350 nm light. e) Response speed of Ag_2Te QD photodiodes with varying device area. f) Response bandwidth of Ag_2Te QD photodiode with varying device area.

solution-processed materials has only been previously reported using perovskites in the near-infrared at 850 nm using a femtosecond amplifier.[24] Our Ag_2Te CQD photodiodes exhibited a fast response time of ≈2.5 ns under 1030 nm femtosecond laser excitation (Figure S16, Supporting Information), similar to previous reports in other materials.[4,15,51] However, this fast response time is in discrepancy with −3 dB bandwidth and response time measurements using low-intensity nanosecond lasers, presumably due to extreme non-equilibrium conditions under intense femtosecond laser excitation.[53,54] Most importantly, the use of femtosecond laser amplifiers is far from a practical implementation setting for LiDAR applications. Therefore, we opted for a commercially available nanosecond diode laser at 1310 nm with a peak power of ≈10 mW, aiming to demonstrate LiDAR in the most eye-safe regime of the SWIR and close to the solar-blind band. **Figure** 5a shows the schematic of a homemade setup for LiDAR demonstration. The laser was modulated with a wavefunction generator to generate laser pulses with ≈30 ns width. The laser pulses were beam-split and referenced with a position-fixed InGaAs detector, while *M1-M5* are movable mirrors to vary the light travel distance before being detected by Ag_2Te CQD PDs. Figure 5b shows the signal transients with different light travel distances by moving mirrors *M1-M5*. Figure 5c shows the contour graphs of signal transients with light travel distances from Ag_2Te QD PDs. The signals showed clear shifts with light travel distance changing and the slope matched well with the light speed. The LiDAR distance resolution with 30 ns laser pulses was further estimated to be at the decimetre level for distances over 10 m, by measuring multiple times at different positions (Figure 5d–f).[24] We believe that higher laser power and shorter laser pulses would further improve depth and distance resolution.

2. Conclusion

In conclusion, we have disclosed an effective strategy to improve surface passivation of Ag_2Te CQDs with tight-binding ligands. The doping levels of Ag_2Te CQD films were further engineered by introducing a novel cationic ligand $AgNO_3$, enabling us with well-controlled doping and improved band-alignment in SWIR photodiodes. The SWIR PDs reached a low dark current of 450 nA cm^{-2} at −0.5 V, EQE over 30%, wide LDR over 150 dB, and a fast response time ≈25 ns. A proof-of-concept SWIR LiDAR was further demonstrated with decimetre level resolution using RoHS-compliant, solution-processed Ag_2Te CQD photodetectors.

3. Experimental Section

Synthesis and Post-Treatment of Ag_2Te Quantum Dots: Ag_2Te QDs were synthesized following our previous report. Briefly, silver iodide-oleylamine

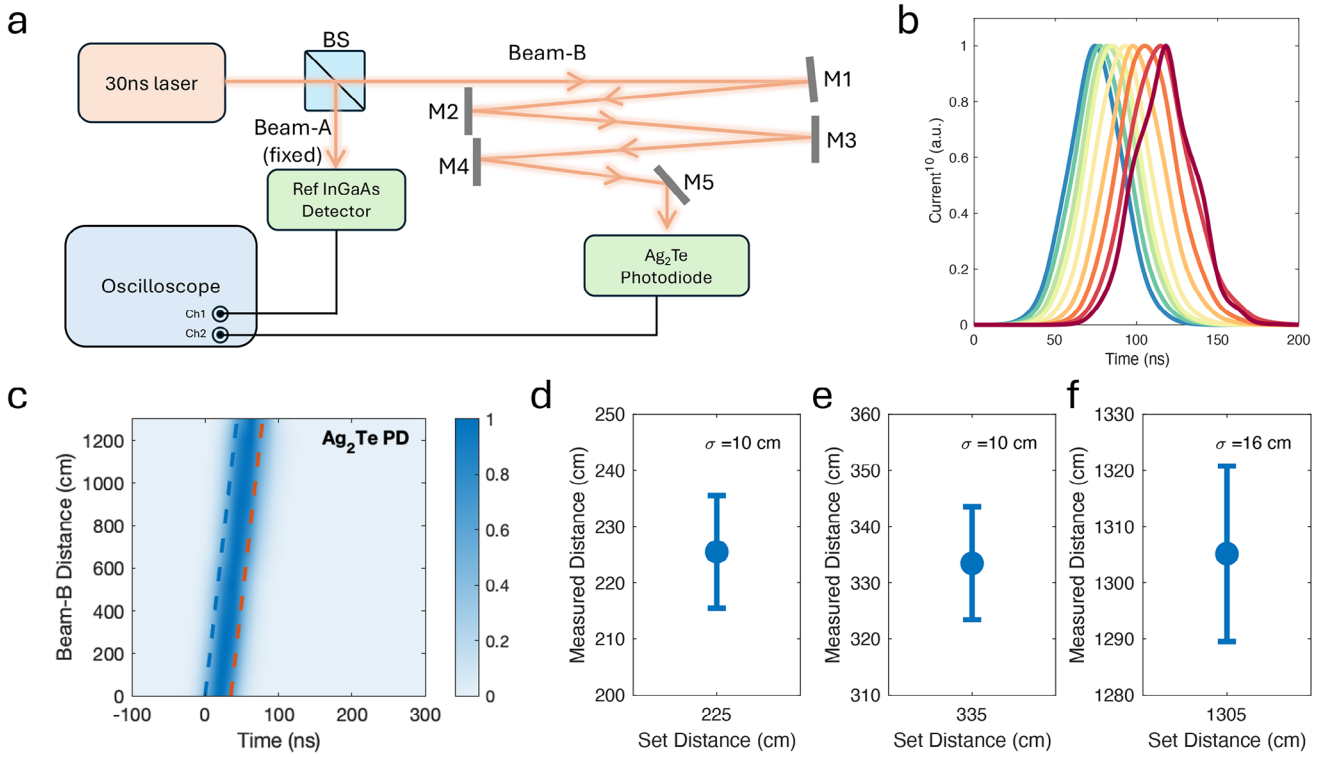

Figure 5. SWIR light detection and ranging (LiDAR) demo. a) Schematic of the homemade LiDAR set-up. b) Signal transients from Ag_2Te QD photodiodes with varying light travel distances. c) Contour plot of the signal transient from Ag_2Te QD photodiodes. d–f) Statistics of measured distances from Ag_2Te QD LiDAR.

(AgI-OLAm) and tellurium oxide-dodecanethiol (TeO_2-DDT) were used as Ag and Te precursors respectively. AgI-OLAm precursor was prepared by dissolving 10 mmol AgI into 10 mL pre-dried OLAm at room temperature under an inert atmosphere. The TeO_2-DDT precursor was prepared by dissolving 2.5 mmol tellurium oxide (TeO_2) into 10 mL dodecanethiol (DDT) under 100 °C heating and an inert atmosphere. Typically, 30 mL oleylamine (OLAm) and 15 mL ODE were loaded into a three-neck flask and pumped at 100 °C to remove oxygen and moisture. The flask was then switched into an argon atmosphere and heated up to 130 °C. Once the temperature reached the set point, 3 mL AgI–OLAm precursor was added to the flask. After ≈5 min, 5 mL TeO_2–DDT precursor was swiftly injected into the flask. The precursor immediately changed into a dark-black color, indicating the nucleation of Ag_2Te QDs. After 5 min, the heating was stopped and left to cool down naturally.

For *OLAm* samples, a crude solution was then transferred into an inert-gas-filled glovebox for purification. Methanol was added into the crude solution to precipitate the QDs, followed by centrifugation. The solid pellet was then fully dispersed into ≈30 mL toluene. Then, 3 mL AgI–OLAm precursor was added into the QD solution, followed by centrifugation to remove any precipitates. Thereafter, ≈15 mL of methanol was added into the supernatant, followed by centrifugation again. The precipitate was discarded and the supernatant, in which the QDs were present, was kept. Further, ≈30 mL of methanol was added into the solution to fully precipitate the QDs, followed by centrifugation. Finally, the solid pellet was collected, and the supernatant was discarded. The QD solid was dissolved into anhydrous toluene at various concentrations for further characterization and device fabrication.

For MPA-OLAm treated QDs, 9 mL MPA was added into the crude solution with a syringe pump. The QD solution was left stirring overnight and then transferred into a glovebox for purification. Methanol was added as an anti-solvent and the QDs were precipitated by centrifugation. QD pellets were further dissolved into a solution containing 30 mL toluene, 4.5 mL OLAm, and 1.5 mL MPA. The QDs were then precipitated by adding methanol and centrifuge once again. The final QD pellets were dissolved into anhydrous toluene for further characterization and device fabrication.

Characterization of Ag_2Te QDs: UV–vis absorption measurements were performed with a Cary 5000 UV-vis-NIR spectroscope in solution. For photoluminescence measurements, a four-channel Thorlabs laser was used as the excitation light and a Kymera 328i spectrograph (Oxford Instruments, Andor) was used as the detector. The PLQY was measured following published methods.[17,55,56] Both excitation and emission spectra were measured and integrated under three different conditions: 1) the sample directly illuminated by the excitation beam in the integrating sphere (S_{dir_ex}, S_{dir_em}); 2) the sample offset from the beam path (indirect excitation) in integrating sphere (S_{indir_ex}, S_{indir_em}); and 3) excitation laser in integrating sphere without sample (S_{0_ex}). The PLQY was further calculated as:

$$PLQY = \frac{S_{dir\_em} + \left(1 - \frac{S_{dir\_ex}}{S_{indir\_ex}}\right) \times S_{indir\_em}}{\left(1 - \frac{S_{dir\_ex}}{S_{indir\_ex}}\right) \times S_{0\_ex}} \quad (2)$$

TEM was performed at the Scientific and Technological Centres of the University of Barcelona. The TEM samples were prepared by dropping a diluted QD solution on ultrathin carbon grids. The X-ray photoelectron spectroscopy/UV photoelectron spectroscopy (XPS/UPS) was performed with a SPECS PHOIBOS 150 hemispherical analyzer under ultrahigh-vacuum conditions (10^{-10} mbar) at the Institut Català de Nanociència i Nanotecnologia. The transient absorption spectroscopy was conducted using a mode-locked Ti: Sapphire femtosecond laser (45 fs) operating at 800 nm and a repetition rate of 1 kHz. An optical parametric amplifier was used to tune the pump wavelength, and the pump fluence was controlled by

a neutral density filter. To control the delay time between the pump and probe, a precise motorized stage was used.

Device Fabrication: All the device fabrication steps were carried out in ambient air unless otherwise mentioned specifically. ITO-covered glass substrates (Universität Stuttgart, Institut für Großflächige Mikroelektronik) were cleaned by sonication in soapy water, acetone, and isopropanol for 20 min each and dried with nitrogen, followed by 0.5 h of UV/ozone treatment. A SnO_2 electron transport layer was then spin-coated from nanoparticle dispersion to form a layer of ≈30 nm, following the reported method. Four layers (≈140 nm) of Ag_2Te QDs were further deposited. For each Ag_2Te QD layer, 50 mg mL^{-1} QD solution was spin coated at 3000 r.p.m. and ligand-exchanged with 1,2-ethanedithiol/acetonitrile (0.1%) or $AgNO_3$/acetonitrile (30 mg mL^{-1}) for 30 s, followed by rinsing twice with acetonitrile and once with toluene, to obtain Ag_2Te-EDT or Ag_2Te-$AgNO_3$ QD films, respectively. For $AgNO_3$ + EDT films, QDs were treated with $AgNO_3$/ACN, and rinsed with ACN/toluene, followed by additional steps of EDT/ACN treatment and ACN/toluene rinses. Finally, a Kurt J. Lesker NANO 36 system was used to deposit 100 nm Au as the top electrodes.

Device Characterization: All the device characterizations were performed in air under ambient conditions. Current–voltage (*J–V*) measurements were performed with a Keysight semiconductor parameter analyzer (B1500A) with the devices kept in a shield box. The EQE value was measured using a Newport Cornerstone 260 monochromator, a Thorlabs MC2000 chopper, a Stanford Research SR570 transimpedance amplifier, and a Stanford Research SR830 lock-in amplifier. Calibrated Newport 818-UV and 818-IR photodetectors were used as the reference. To measure the 3 dB bandwidth, a nanosecond laser was used as incident light, which was modulated by a waveform generator (Agilent 33220A) at various frequencies with a 50% duty cycle. The output current was recorded with an oscilloscope. For LDR measurements, a four-channel laser (Thorlabs) at 1310 nm was used as the light source. The light was directed by a beam-splitter to a Newport 818-IG detector and the device. The current was then measured by a semiconductor parameter analyzer.

LiDAR Demo: For the light detection and ranging (LiDAR) demo, a 1310 nm laser with a peak power of ≈10 mW was controlled with an Agilent wave function generator at a frequency of 10 kHz and pulse width of 30 ns. The currents from devices were amplified with a variable gain high bandwidth preamplifier and collected with an oscilloscope. The current transients were further processed to remove ringing artifacts and multiplied by a power of 10 for better visualizing the peak positions.[24]

Supporting Information

Supporting Information is available from the Wiley Online Library or from the author.

Acknowledgements

Y.W. and H.W. contributed equally to this work. G.K. acknowledges financial support from the European Research Council (ERC) under the European Union's Horizon 2020 research and innovation programme (grant agreement no. 101002306), the Fundació Privada Cellex, the program CERCA and "Severo Ochoa" Centre of Excellence CEX2019-000910-S funded by the Spanish State Research Agency. This project had also received funding from the European Union under grant agreement No 101119489. Views and opinions expressed are however those of the author(s) only and do not necessarily reflect those of the European Union. Neither the European Union nor the granting authority can be held responsible for them. C.R. acknowledges MCIU (Ministerio de Ciencia Innovacion y Universidades)/AEI(Agencia Estatal de Investigacion)/10.13039/501100011033 and European Union "NextGenerationEU"/PRTR under the Juan de La Cierva fellowship JDC2022-049722-I.

Conflict of Interest

G.K. serves as co-founder, share-holder and scientific advisor at Qurv.

Data Availability Statement

The data that support the findings of this study are available from the corresponding author upon reasonable request.

Keywords

colloidal quantum dots, infrared, LiDAR, photodetectors, silver telluride

Received: January 14, 2025
Revised: February 25, 2025
Published online: March 31, 2025

[1] N. C. Ahlquist, R. J. Charlson, *Atmos. Environ.* **1969**, *3*, 551.
[2] H. Yang, Z. Ma, Q. Wang, *ACS Nano* **2024**, *18*, 30123.
[3] T. J. T. P. van den Berg, H. Spekreijse, *Vision Res.* **1997**, *37*, 249.
[4] Y.-H. Deng, C. Pang, E. Kheradmand, J. Leemans, J. Bai, M. Minjauw, J. Liu, K. Molkens, J. Beeckman, C. Detavernier, P. Geiregat, D. Van Thourhout, Z. Hens, *Adv. Mater.* **2024**, *36*, 2402002.
[5] Z. Liu, C. Hao, Y. Liu, R. Wu, J. Zhang, Z. Chen, F. Wang, L. Guan, X. Li, A. Tang, O. Chen, *ACS Nano* **2024**, *18*, 21523.
[6] S. A. McDonald, G. Konstantatos, S. Zhang, P. W. Cyr, E. J. D. Klem, L. Levina, E. H. Sargent, *Nat. Mater.* **2005**, *4*, 138.
[7] Y. Wang, Z. Liu, N. Huo, F. Li, M. Gu, X. Ling, Y. Zhang, K. Lu, L. Han, H. Fang, A. G. Shulga, Y. Xue, S. Zhou, F. Yang, X. Tang, J. Zheng, M. Antonietta Loi, G. Konstantatos, W. Ma, *Nat. Commun.* **2019**, *10*, 5136.
[8] G. Konstantatos, I. Howard, A. Fischer, S. Hoogland, J. Clifford, E. Klem, L. Levina, E. H. Sargent, *Nature* **2006**, *442*, 180.
[9] J. Yang, H. Hu, Y. Lv, M. Yuan, B. Wang, Z. He, S. Chen, Y. Wang, Z. Hu, M. Yu, X. Zhang, J. He, J. Zhang, H. Liu, H.-Y. Hsu, J. Tang, H. Song, X. Lan, *Nano Lett.* **2022**, *22*, 3465.
[10] K. A. Sergeeva, H. Zhang, A. S. Portniagin, E. Bossavit, G. Mu, S. V. Kershaw, S. Ithurria, P. Guyot-Sionnest, S. Keuleyan, C. Delerue, X. Tang, A. L. Rogach, E. Lhuillier, *Adv. Funct. Mater.* **2024**, *34*, 2405307.
[11] X. Tang, M. M. Ackerman, M. Chen, P. Guyot-Sionnest, *Nat. Photonics* **2019**, *13*, 277.
[12] H. W. Ban, M. Vafaie, L. Levina, P. Xia, M. Imran, Y. Liu, A. M. Najarian, E. H. Sargent, *J. Am. Chem. Soc.* **2024**, *146*, 24935.
[13] P. Xia, B. Sun, M. Biondi, J. Xu, O. Atan, M. Imran, Y. Hassan, Y. Liu, J. M. Pina, A. M. Najarian, L. Grater, K. Bertens, L. K. Sagar, H. Anwar, M.-J. Choi, Y. Zhang, M. Hasham, F. P. García de Arquer, S. Hoogland, M. W. B. Wilson, E. H. Sargent, *Adv. Mater.* **2023**, *35*, 2301842.
[14] T. Sheikh, W. J. Mir, A. Alofi, M. Skoroterski, R. Zhou, S. Nematulloev, M. N. Hedhili, M. B. Hassine, M. S. Khan, K. E. Yorov, B. E. Hasanov, H. Liao, Y. Yang, A. Shamim, M. Abulikemu, O. F. Mohammed, O. M. Bakr, *J. Am. Chem. Soc.* **2024**, *146*, 29094.
[15] B. Sun, A. M. Najarian, L. K. Sagar, M. Biondi, M.-J. Choi, X. Li, L. Levina, S.-W. Baek, C. Zheng, S. Lee, A. R. Kirmani, R. Sabatini, J. Abed, M. Liu, M. Vafaie, P. Li, L. J. Richter, O. Voznyy, M. Chekini, Z.-H. Lu, F. P. García de Arquer, E. H. Sargent, *Adv. Mater.* **2022**, *34*, 2203039.
[16] Muhammad, D. C., D. H. Parmar, B. Rehl, Y. Zhang, O. Atan, G. Kim, P. Xia, J. M. Pina, M. Li, Y. Liu, O. Voznyy, S. Hoogland, E. H. Sargent, *Adv. Mater.* **2023**, *35*, 2306147.
[17] L. Peng, Y. Wang, Y. Ren, Z. Wang, P. Cao, G. Konstantatos, *ACS Nano* **2024**, *18*, 5113.
[18] H. Seo, H. J. Eun, A. Y. Lee, H. K. Lee, J. H. Kim, S.-W. Kim, *Adv. Sci.* **2024**, *11*, 2306439.
[19] Y. Ahn, S. Y. Eom, G. Kim, J. H. Lee, B. Kim, D. Kim, M.-J. Si, M. Yang, Y. Jung, B. S. Kim, Y. J. Chung, K. S. Jeong, S.-W. Baek, *Adv. Sci.* **2024**, *11*, 2407453.

[20] G. Kim, D. Choi, S. Y. Eom, E. D. Jung, J. H. Lee, B. Rehl, S. Y. Kim, S. Hoogland, E. H. Sargent, K. S. Jeong, *ACS Mater. Lett.* **2024**, *6*, 4988.
[21] Y. Wang, L. Peng, J. Schreier, Y. Bi, A. Black, A. Malla, S. Goossens, G. Konstantatos, *Nat. Photonics* **2024**, *18*, 236.
[22] C. Liao, L. Tang, Y. Jia, S. Sun, H. Yang, J. Xu, Z. Gu, *Nano Lett.* **2023**, *23*, 9865.
[23] R. Bera, M. Dosil, G. Konstantatos, *Nano Lett.* **2024**, *24*, 13919.
[24] A. Morteza Najarian, M. Vafaie, A. Johnston, T. Zhu, M. Wei, M. I. Saidaminov, Y. Hou, S. Hoogland, F. P. García De Arquer, E. H. Sargent, *Nat. Electron.* **2022**, *5*, 511.
[25] J. De Roo, M. Ibáñez, P. Geiregat, G. Nedelcu, W. Walravens, J. Maes, J. C. Martins, I. Van Driessche, M. V. Kovalenko, Z. Hens, *ACS Nano* **2016**, *10*, 2071.
[26] S. Gallagher, J. Kline, F. Jahanbakhshi, J. C. Sadighian, I. Lyons, G. Shen, B. F. Hammel, S. Yazdi, G. Dukovic, A. M. Rappe, D. S. Ginger, *ACS Nano* **2024**, *18*, 19208.
[27] L. De Trizio, I. Infante, L. Manna, *Acc. Chem. Res.* **2023**, *56*, 1815.
[28] C. C. Reinhart, E. Johansson, *J. Am. Chem. Soc.* **2017**, *139*, 5827.
[29] M. Gu, Y. Wang, F. Yang, K. Lu, Y. Xue, T. Wu, H. Fang, S. Zhou, Y. Zhang, X. Ling, Y. Xu, F. Li, J. Yuan, M. A. Loi, Z. Liu, W. Ma, *J. Mater. Chem. A* **2019**, *7*, 15951.
[30] W. J. Mir, T. Sheikh, S. Nematulloev, P. Maity, K. E. Yorov, A.-H. Emwas, M. N. Hedhili, M. S. Khan, M. Abulikemu, O. F. Mohammed, O. M. Bakr, *Small* **2024**, *20*, 2306535.
[31] C. T. Smith, M. A. Leontiadou, R. Page, P. O'Brien, D. J. Binks, *Adv. Sci.* **2015**, *2*, 1500088.
[32] X. Jiang, Z. Zang, Y. Zhou, H. Li, Q. Wei, Z. Ning, *Acc. Mater. Res.* **2021**, *2*, 210.
[33] L. Gregori, D. Meggiolaro, F. De Angelis, *Small* **2024**, 20, 2403413.
[34] Y. Deng, Z. Ni, A. F. Palmstrom, J. Zhao, S. Xu, C. H. Van Brackle, X. Xiao, K. Zhu, J. Huang, *Joule* **2020**, *4*, 1949.
[35] C. R. Kagan, E. Lifshitz, E. H. Sargent, D. V. Talapin, *Science* **2016**, *353*, aac5523.
[36] M. N. An, S. Y. Eom, J. H. Lee, H. Song, M. Cho, K. S. Jeong, *ACS Appl. Nano Mater.* **2023**, *6*, 22488.
[37] H. Song, J. H. Lee, S. Y. Eom, D. Choi, K. S. Jeong, *ACS Nano* **2023**, *17*, 16895.
[38] R. H. Gilmore, Y. Liu, W. Shcherbakov-Wu, N. S. Dahod, E. M. Y. Lee, M. C. Weidman, H. Li, J. Jean, V. Bulović, A. P. Willard, J. C. Grossman, W. A. Tisdale, *Matter* **2019**, *1*, 250.
[39] N. Taghipour, G. L. Whitworth, A. Othonos, M. Dalmases, S. Pradhan, Y. Wang, G. Kumar, G. Konstantatos, *Adv. Mater.* **2022**, *34*, 2107532.
[40] C. R. Kagan, C. B. Murray, *Nat. Nanotechnol.* **2015**, *10*, 1013.
[41] S. Kahmann, M. A. Loi, *Appl. Phys. Rev.* **2020**, *7*, 041305.
[42] J.-H. Choi, A. T. Fafarman, S. J. Oh, D.-K. Ko, D. K. Kim, B. T. Diroll, S. Muramoto, J. G. Gillen, C. B. Murray, C. R. Kagan, *Nano Lett.* **2012**, *12*, 2631.
[43] D. Chen, Y. Liu, B. Xia, L. Chen, Y. Yang, G. Yang, J. Liu, S. Lu, C. Ge, P. Liu, J. Yang, G. Liang, X. Lan, X. Zeng, L. Li, J. Zhang, Z. Xiao, L. Gao, J. Tang, *Adv. Funct. Mater.* **2023**, *33*, 2210158.
[44] M. J. Speirs, D. N. Dirin, M. Abdu-Aguye, D. M. Balazs, M. V. Kovalenko, M. A. Loi, *Energy Environ. Sci.* **2016**, *9*, 2916.
[45] J. P. Clifford, K. W. Johnston, L. Levina, E. H. Sargent, *Appl. Phys. Lett.* **2007**, *91*, 253117.
[46] J. Liu, P. Liu, D. Chen, T. Shi, X. Qu, L. Chen, T. Wu, J. Ke, K. Xiong, M. Li, H. Song, W. Wei, J. Cao, J. Zhang, L. Gao, J. Tang, *Nat. Electron.* **2022**, *5*, 443.
[47] B. Wang, M. Yuan, J. Liu, X. Zhang, J. Liu, J. Yang, L. Gao, J. Zhang, J. Tang, X. Lan, *Nano Lett.* **2024**, *24*, 9583.
[48] M. Imran, D. B. Kim, P. Xia, F. Y. Villanueva, B. Rehl, J. M. Pina, Y. Liu, Y. Zhang, O. Voznyy, E. Kumacheva, S. Hoogland, E. H. Sargent, *Adv. Mater.* **2025**, *37*, 2420273.
[49] B. K. Jung, H. Yoo, B. Seo, H. J. Choi, Y. K. Choi, T. H. Kim, N. Oh, S. Y. Kim, S. Kim, Y. Lee, J. W. Shim, H. Y. Park, G. W. Hwang, T. N. Ng, S. J. Oh, *ACS Energy Lett.* **2024**, *9*, 504.
[50] Y. Zhang, P. Xia, B. Rehl, D. H. Parmar, D. Choi, M. Imran, Y. Chen, Y. Liu, M. Vafaie, C. Li, O. Atan, J. M. Pina, W. Paritmongkol, L. Levina, O. Voznyy, S. Hoogland, E. H. Sargent, *Angew. Chem.* **2024**, *136*, 202316733.
[51] M. Vafaie, J. Z. Fan, A. M. Najarian, O. Ouellette, L. K. Sagar, K. Bertens, B. Sun, F. P. G. de Arquer, E. H. Sargent, *Matter* **2021**, *4*, 1042.
[52] N. Na, Y.-C. Lu, Y.-H. Liu, P.-W. Chen, Y.-C. Lai, Y.-R. Lin, C.-C. Lin, T. Shia, C.-H. Cheng, S.-L. Chen, *Nature* **2024**, *627*, 295.
[53] Z. Zhang, J. Sung, D. T. W. Toolan, S. Han, R. Pandya, M. P. Weir, J. Xiao, S. Dowland, M. Liu, A. J. Ryan, R. A. L. Jones, S. Huang, A. Rao, *Nat. Mater.* **2022**, *21*, 533.
[54] M. Liu, S. D. Verma, Z. Zhang, J. Sung, A. Rao, *Nano Lett.* **2021**, *21*, 8945.
[55] J. C. de Mello, H. F. Wittmann, R. H. Friend, *Adv. Mater.* **1997**, *9*, 230.
[56] Y.-K. Wang, H. Wan, S. Teale, L. Grater, F. Zhao, Z. Zhang, H.-W. Duan, M. Imran, S.-D. Wang, S. Hoogland, L.-S. Liao, *Nature* **2024**, *629*, 586.